buildings

MDPI

Article

Up-Floating Destruction and Reinforcement Measures of Damaged Basement Based on the Bending Moment and Deformation Analysis

Zhifeng Wu [1,2], Zhiyong Li [2,3,*], Jian Fan [1], Hongyou Cao [2], Bo Huang [2,4] and Hui Liu [2,4]

1 School of Civil and Hydraulic Engineering, Huazhong University of Science and Technology, Wuhan 430074, China
2 School of Civil Engineering & Architecture, Wuhan University of Technology, Wuhan 430070, China
3 Wuhan University of Technology Design & Research Institute Co., Ltd., Wuhan 430070, China
4 Hainan Institute of Wuhan University of Technology, Sanya 572025, China
* Correspondence: lzy2003@whut.edu.cn

Abstract: Based on the up-floating incident of the basement in a high-rise residential building, the finite element (FE) model of the up-floating destruction region is established to investigate the damage mechanism. The stress states and the deformations of the basement structure are obtained under complex loads including water buoyancy forces, vehicle loads and construction loads. To assess the extent of damage, a novel damage indicator is defined based on two levels: the cracking bending moments and the yield bending moment. The first-level cracking bending moment, second-level cracking bending moment and the yield bending moment can be determined using the section stratification method. By comparing the maximum bending moment of the component with its corresponding cracking moment, one can determine whether the cracks have occurred and assess their severity. Meanwhile, the antifloating failure model is constructed to analyze the mechanism of the up-floating destruction. Finally, a detailed reinforcement treatment plan of 'decompression first and then reinforcement' is presented to reinforce and repair the damaged basement structure. The mechanism analysis of the up-floating destruction and the comprehensive reinforcement treatments ensure the simulation of the life cycle of emergence, development and treatment to ensure structural safety.

Keywords: up-floating destruction; damage mechanism; cracking bending moment; decompression; reinforcement

check for updates

Citation: Wu, Z.; Li, Z.; Fan, J.; Cao, H.; Huang, B.; Liu, H. Up-Floating Destruction and Reinforcement Measures of Damaged Basement Based on the Bending Moment and Deformation Analysis. *Buildings* **2023**, *13*, 1918. https://doi.org/10.3390/buildings13081918

Academic Editor: Alberto Taliercio

Received: 22 June 2023
Revised: 24 July 2023
Accepted: 24 July 2023
Published: 28 July 2023

Copyright: © 2023 by the authors. Licensee MDPI, Basel, Switzerland. This article is an open access article distributed under the terms and conditions of the Creative Commons Attribution (CC BY) license (https://creativecommons.org/licenses/by/4.0/).

1. Introduction

Tsunamis [1–3], strong winds [4], earthquakes [5] and fire [6] disasters are the usual risks considered by designers and engineers to maintain the safety and reliability of building structures and underground structures. Due to the impact of tsunamis, the self-weight of the structure is insufficient to withstand the static and dynamic forces exerted by the water on them [1–3]. Except for tsunamis, there are other hazards that can cause the structures to float, such as floods [7,8], tidal water from the sea and swollen river water. Due to intense and heavy rainfall, excessive and rapid water may lead to unforeseen changes in the water table. Therefore, these hazards caused by extreme and soaring water tables have become critical issues that designers and engineers must consider [9].

Unlike extreme tsunamis and floods, the unexpected rise in water levels during the rainy season is a more common reason for compromising the safety and stability of underground structures, as well as the overall reliability of building structures [10]. The buoyancy forces exerted by the high-level underground water can result in uplift bulging effects and even lead to the destruction of large-scale underground structures [11–19], such as the tunnels [12], caissons [13], passages and shopping malls [14,15] and garages of high-rise buildings [18]. Therefore, reasonable antifloating design and construction of underground structures are significantly important.

With the increasing development of underground structures in the vertical direction, the current description of water buoyancy and antifloating measures are insufficient to ensure structural safety. The uplift destruction and cracks of underground structures and buildings continue to occur intermittently. Murat Bikce et al. [17] found that the buoyancy forces of a flood caused damage to an office building in Hatay/Turkey during construction. The water rushed into the excavation region, creating a closed volume similar to a pool in the damaged area. The water buoyancy forces on this structure exceeded its total weight, resulting in the up-floating and consequent damages. Zhu et al. [18] developed a FE model to investigate the causes of cracks in the bottom floor of an underground garage. The primary factor is attributed to the uplift force generated by the underground water and expansive soil. Maj et al. [19] identified the causes of cracks and dampness in a multi-story underground garage as resulting from inadequate antifloating measures during the design stage. Fu et al. [20] discovered that any deviation in the understanding of antifloating design can result in issues such as the motherboard cracking or basement floating, which are still prevalent in engineering projects. Therefore, it is imperative to ensure the antifloating stability of underground structures in high-rise buildings during both the construction and service stages.

Furthermore, once the issue of floating arises, it is necessary to consider designing higher-quality antifloating measures and reinforcement treatments. To counteract the hydrostatic uplift, various methods have been proposed by researchers. Maulik et al. [21] suggest that the installation of piles at the bottom of basement slabs is the most effective approach, while Wong [22] recommends using tension piles and a water pressure relief system beneath the base slab of the basement structure. Srivastava et al. [23] advocate for anchor pile installation below basement rafts to prevent uplift caused by seepage pressure from high groundwater tables. Yang et al. [24] employed the novel antifloating anchor and reinforced concrete slab to enhance both the overall and partial antiuplift capacity of the structural underground components. Zhu et al. [25] developed an interception and drainage antifloating system as a substitute for the reconstruction of uplift piles or anchors, which can effectively prevent blind water drainage. The system involves constructing a cutoff wall around the underground structures to intercept water and setting several relief wells on the bottom slab to drain water. Even Li et al. [26] have implemented an automated drainage system to replace the previous antifloating anchor rod technology, while Tang et al. [27] conducted an analysis of the underground garage's floating phenomenon caused by rainstorms and proposed several corresponding reinforcement measures for damaged members such as slabs, beams, columns and piles. Similarly, Zhang [28] and Huang et al. [29] attributed the cracks observed in basement floors, walls, beams and columns to water buoyancy forces resulting from precipitation. They implemented comprehensive reinforcement measures for damaged members.

In light of the aforementioned literature on the uplift damage and reinforcement measures, an investigation into the antifloating failure accident of a high-rise residential building's basement was conducted. Initially, a FE model of the uplift damaged area in the basement structure under complex loads from the water buoyancy, vehicle traffic and construction activities was established by ANSYS. To evaluate the degree of damage, a novel damage indicator was defined based on the two levels of the cracking bending moments and the yield bending moment to determine the state of cracks. The section stratification method can be used to determine these values. By comparing the maximum bending moment with the corresponding cracking moment, it is possible to judge whether or not the components have developed cracks. Meanwhile, an antifloating failure model was developed to analyze the mechanism of destruction caused by the up-floating. Finally, a detailed reinforcement treatment scheme of 'decompression first and then reinforcement' is presented to strengthen and repair the basement structure that has suffered from the uplift destruction.

2. Examination of the Damaged Basement

The project example concerns a damaged basement of a high-rise commercial and residential building with a framed shear wall structure for the use of parking and fire escapes in the district, which is located in a city in southern China. The structural schematic diagram of the basement and the affected area of the damaged basement are depicted in Figure 1. The length of the destruction area measures 80 m along the X-axis and 33 m along the Y-axis. The dimensions and material parameters of the top and bottom slabs of the basement are presented in Table 1. The top slabs of the basement have been partially reinforced, with a designed overburden thickness of 0.8 m. The concrete pad beneath the basement floor has a compressive strength of C30 and a thickness of 0.1 m, while the basement walls and columns have a higher strength rating of C40. The foundation, beams and sidewalls also possess considerable strength with a rating of C30. Notably, the thickness of the basement sidewalls measures 0.3 m.

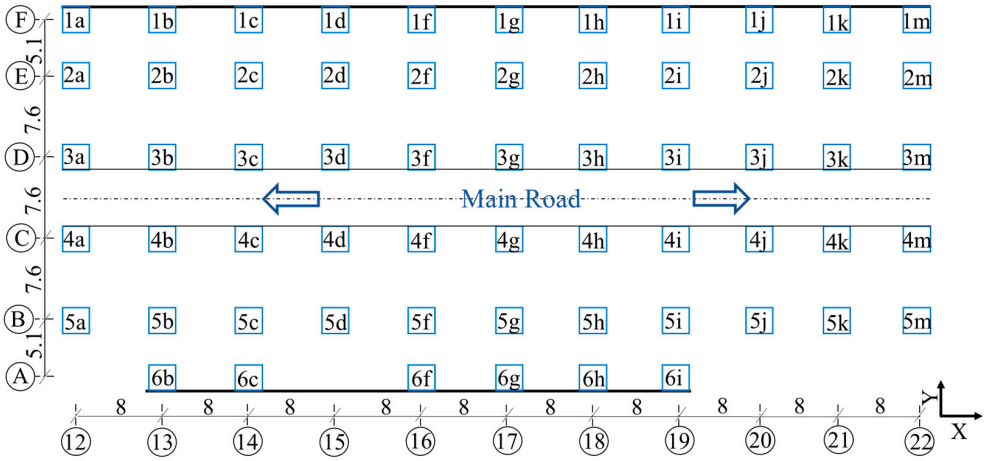


Figure 1. The destruction area in the basement: blue square means the initial intact column. 1a indicates the number of the column. According to architectural drawing codes, A denotes the A-axis along the X-axis, and 12 represents the 12-axis along the Y-axis. The unit of the distance is meter (m). Blue arrows are the directions of main road.

Table 1. The dimensions and material parameters of the top and bottom slabs of the basement.

Components	Designed Elevation (m)	Thickness (m)	Designed Strength of Concrete	Reinforcement at the Top and Bottom Slab
Top slab	−1.95	0.16	C30	ϕ10 @175(Bidirectional) + ϕ10 @200(Bidirectional)
Bottom slab	−5.90	0.40	C30	ϕ8 @200(Bidirectional) + ϕ8 @200(Bidirectional)

The basement structure pertains to the foremountain alluvial fan geomorphic. The site is level, unobstructed and relatively low-lying. Based on the survey findings, within the drilling depth range, the quaternary strata exposed at this location primarily comprise fill, alluvium and eluvium as well as granite bedrock. The groundwater at the site is of the upper stage-pore diving type, which exists within the pores of quaternary soil layers. The water-rich strata consist of fine and medium coarse sand. The groundwater recharge occurs through atmospheric precipitation infiltration, while discharge takes place via evaporation. The buried depth of the underground static water level at the site ranges from 1.12 to 1.58 m, with an average of 1.31 m, which is approximately equivalent to elevations ranging from 0.60 to 1.72 m and an average elevation of 1.18 m. The stable water level experiences seasonal fluctuations with a typical amplitude of ±0.50 m due to climatic influences. The fine sand and medium coarse sand layers present on-site are classified as strong permeable strata while other soil layers exhibit weak-micro permeability. It is advisable to utilize

the design elevation of the outdoor flooring system as a reference for determining the antifloating water level of the basement.

According to the on-site inspection, a significant number of reinforced concrete walls and columns in the basement exhibit cracks, primarily concentrated within Axes 12–22 and Axes A–F as depicted in Figure 2. At the onset of the cracking, only a limited number of fissures appear on the walls and columns with minimal degrees of severity. As cracks progress, their quantity increases while damage intensifies. After further development, the number of cracks increases and their severity worsens. The cracks mainly take a horizontal form and penetrate partially through the cross-section of the column. Additionally, a few cracks exhibit the full-sectional penetration. Based on the severity of the damage, these cracks can be categorized into four levels (Levels A, B, C and D) with the increasing degrees of cracking as illustrated in Figure 3. Between Axis 14 and Axis 22, a total of 47 columns displayed significant cracks. Among them, Level C cracks were observed in 20 columns. The columns on Axis 12 and Axis 13 do not exhibit any observed cracks. The majority of cracks are between Level B and Level C, situated at the bottom and top of the columns and oriented towards adjacent high-rise buildings. Columns located in close proximity to high-rise residential buildings, such as those on Axes B, C, E and F, display more severe degrees of cracking when compared to those on Axis D. Some cracks with a diagonal upward orientation of 45° appear at the intersections between the columns situated on the outer sidewalls and the beams of the top slab. These cracks have progressed to damage of Level D, with widths exceeding 2 mm and lengths in excess of 1 m for certain columns.

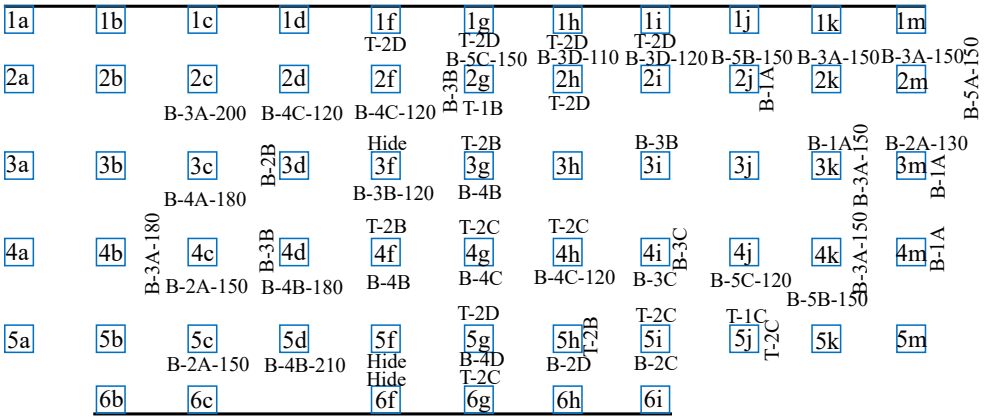
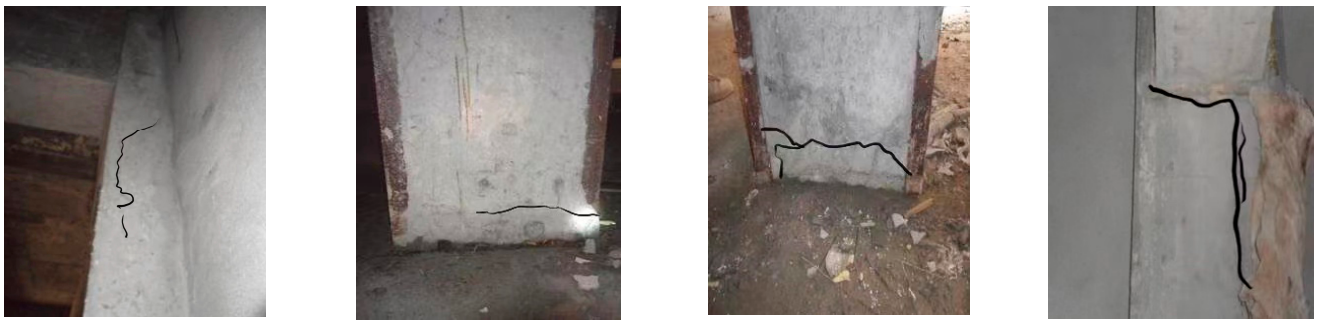


Figure 2. The cracks at the damaged columns: B-3A-200 indicates three cracks of Level A with a distance of 200 mm at the column bottom. T-2D denotes two cracks of Level D at the column top.

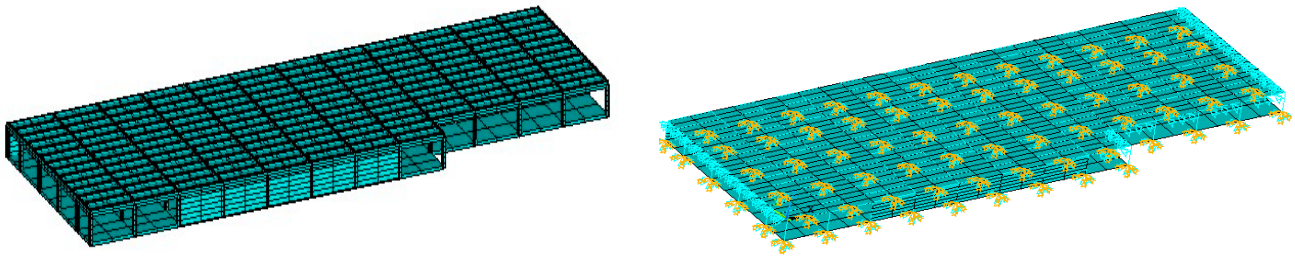


(**a**) (**b**) (**c**) (**d**)

Figure 3. Four levels of cracks, namely A, B, C and D, based on the degrees of cracking. (**a**) Level A: The minuscule vertical fissures located at the center of the column. (**b**) Level B: The minute horizontal fissures that traverse the partial cross-section of the column bottom. (**c**) Level C: The horizontal cracks that traverse the entire cross-section of the column bottom. (**d**) Level D: The horizontal and vertical cracks that traverse the entire cross-section of the column top.

3. FE Analysis of the Basement

To simulate damage scenarios of the basement and analyze the causes of cracking, an FE model of the damaged area is constructed by ANSYS as shown in Figure 4a. The X-direction length between Axis 12 and Axis 22 is 80 m, while the Y-direction distance from Axis A to Axis F is 33 m. The net height of the basement in the Z-direction is 3.7 m. The material parameters and element types of the initial FE model are listed in Table 2.



(**a**) (**b**)

Figure 4. FE model of the destruction area. (**a**) FE model. (**b**) The constraints.

Table 2. Material parameters and element types of the initial FE model.

Components	Strength	Elastic Modulus (MPa)	Poisson Ratio	Density (kg/m^3)	Sectional Parameters	Element Type
Column	C40	32.5	0.3	2500	0.5 × 0.5 × 0.3 m^3	Beam 188
Longitudinal beam (X-axis)	C30	30	0.3	2500	0.3 × 0.7 × 8 m^3	Beam 188
Transverse beam (Y-axis)	C30	30	0.3	2500	0.4 × 0.8 × 5.1 m^3/ 0.4 × 0.8 × 7.6 m^3	Beam 188
Top slab	C30	30	0.3	2500	0.16 m (Thickness)	Shell 181
Bottom slab	C30	30	0.3	2500	0.4 m (Thickness)	Shell 181
Side shear wall	C40	32.5	0.3	2500	0.3 m (Height)	Shell 181
Steel	HRB400	360	0.3	7850		Link 8

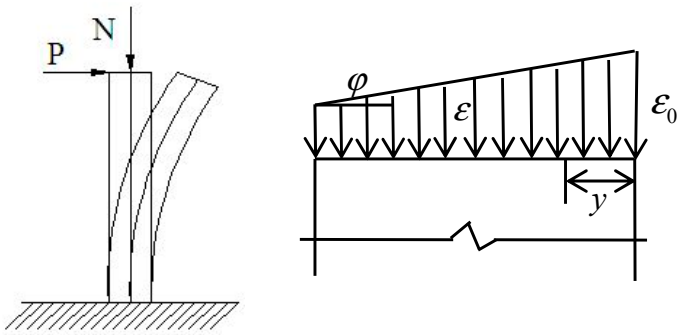
Due to the influence of the adjacent high-rise buildings, the positive restraints in the X-direction can be observed at the top of the columns on Axis 12, while a series of negative restraints in the X-direction are applied to those on Axis 22 to restrict the nodal movement. The initial state of the damaged area is assumed to be intact under normal circumstances. Therefore, apart from these aforementioned nodes, all other nodes at both ends of each column are considered as rigid joints under the action of pile foundation and casing soil. The corresponding constraints of the FE model are illustrated in Figure 4b.

Due to the rising water table during the rainy season in southern regions [30,31], it is preliminarily judged that the significant buoyancy forces will likely occur at the base plate of the basement. Based on the literature sources [32–35], it is assumed that the groundwater level in this project example is 3 m below the standard horizontal level. The buoyancy force exerted on the bottom slab can be equivalent to the vertical upward concentrated force 127.44 kN loaded on all nodes located below the bottom slab. The effect of water buoyancy force on the shear wall is 28.8 kN. Meanwhile, the dead load of the structure is equal to 39.269 kN. The heavy loads can also be equivalent to the vertical downward concentrated load 54.5 kN applied to the nodes on the top slab.

3.1. The Damage Indicator of the Defined Cracking Bending Moment

Before conducting a thorough investigation, the damage indicator for determining the presence of cracking is defined as various levels of bending moments in this section. The first-stage cracking moment (Stage 1) can be determined when the concrete at the outermost edge of the sectional tensile zone reaches the ultimate tensile strain. Once the concrete at

the edge of the hoop reinforcement in the sectional tensile zone reaches its ultimate tensile strain, the corresponding sectional bending moment can be considered as the second-stage cracking moment (Stage 2). The yield bending moment (Stage 3) is a commonly used indicator [36] to determine whether or not the outermost longitudinal reinforcement in the sectional tensile zone has reached its yield tensile strain. When the component is subjected to the bending moment or a combination of bending moment and axial pressure, cracks will appear in the corresponding position of the section once the concrete reaches its ultimate tensile strain. As shown in Figure 5, under the combined action of axial force N and horizontal thrust P, the column exhibits compression and bending deformation. Based on the assumption of a flat cross-section, the normal stress distribution in each section will be linear along the column height direction. This is due to the uniform compression deformation caused by axial force and bending deformation from horizontal thrust.



(**a**) (**b**)

Figure 5. The compressive and flexural deformation of concrete component. (**a**) The deformation of the component. (**b**) Strain distribution of the column cross-section.

According to the equilibrium condition, the relationship between the internal force and the stress can be satisfied as follows:

$$N = \int_A \sigma dA = \int_{A_c} \sigma_c dA + \int_{A_s} \sigma_s dA \tag{1}$$

$$M = \int_A \sigma y dA = \int_{A_c} \sigma_c y dA + \int_{A_s} \sigma_s y dA \tag{2}$$

where N denotes the internal axial force. M represents the sectional moment. A_c and A_s indicate the cross-sectional areas of the concrete and steel, respectively. σ_c and σ_s represent the stress of the concrete and steel, respectively. y is the horizontal coordinate value of the column section relative to the side edge of the compression region.

The stress of the concrete and steel can be determined using the equations above, respectively:

$$\sigma_c = E_c \cdot \varepsilon \tag{3}$$

$$\sigma_s = E_s \cdot \varepsilon \tag{4}$$

where ε indicates the sectional strain, which is determined by the axial compression ε_0 and the curvature φ, as illustrated in Figure 5b, as:

$$\varepsilon = \varepsilon_0 - \varphi y \tag{5}$$

To solve the sectional bending moments in Equations (1) and (2), the section stratification method is introduced for the integral calculation of the equations. The component's section is supposed and divided into multiple layers parallel to the bending axis, with

uniform and constant stress assumed in each layer. The average stress is used to represent the corresponding layer's stress state, allowing for the calculation of both axis force and bending moment. The corresponding axis force and bending moment can be calculated:

$$N = \int_A \sigma dA = \sum_{i=1}^{n} \sigma_{ci} \Delta A_{ci} + \sum_{i=1}^{n'} \sigma_{si} \Delta A_{si} \quad (6)$$

$$M = \int_A \sigma y dA = \sum_{i=1}^{n} \sigma_{ci} y_i \Delta A_{ci} + \sum_{i=1}^{n'} \sigma_{si} y_i \Delta A_{si} \quad (7)$$

where ΔA_{ci} and ΔA_{si} mean the areas of the concrete and steel in the ith layer, respectively. σ_{ci} and σ_{si} indicate the corresponding stresses for the concrete and steel. y_i represents the average coordinate of the ith layer relative to the centroid. n and n' denote the number of layers of the concrete and steel, respectively.

Hence, given the known properties of steel and concrete materials along with section and reinforcement conditions, Equations (1)–(7) can be utilized to determine the cracking moment and yield bending moment of a section subjected to varying axial forces.

In this section, the frame column in the basement is taken as an example. The concrete strength is C40 and the longitudinal bars in the column have a strength of HRB400. The stress–strain relationship of both materials, including concrete and steel, was obtained from the literature [36]. Considering that the KZ2 column type is frequently used, its cross-section and reinforcement forms are shown in Figure 6. According to the load combination specified in Code [37], the design value of axial force controlled by permanent load effect is 736.95 kN. To ensure calculation accuracy, the concrete in the compression zone is divided into 20 layers. Table 3 lists the bending moments at all stages of the KZ2 column under the vehicle loads. Cracks begin to appear when the bending moment reaches the Stage 1 cracking moment of 97.37 kN·m. When the bending moment of the column exceeds the Stage 2 cracking moment of 106.33 kN·m, the concrete protective layer will be penetrated by cracks in the column. Once the bending moment reaches the Stage 3 moment of 265.17 kN·m, these developed cracks will cause plastic deformation in the column.

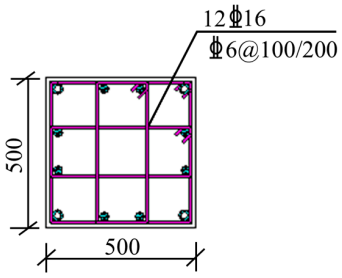


Figure 6. The cross-section and reinforcement of the KZ2 column.

Table 3. The sectional cracking moment and the yield bending moments of the KZ2 column.

Stages of Bending Moment	Calculation Conditions	Axial Force (kN)	Bending Moment (kN·m)
First-stage cracking moment (Stage 1)	The column experienced a pullout failure at its outermost edge. (ε = 0.0001)	736.95	97.37
Second-stage cracking moment (Stage 2)	The occurrence of cracking is observed at the outer edge of the column's protective layer or hoop reinforcement. (ε = 0.0001)	736.95	106.33
Yield bending moment (Stage 3)	The outermost longitudinal reinforcement in the tension zone experienced yielding. (ε = 0.0018)	736.95	265.17

3.2. The Destruction under Varying Vehicle Loads

Furthermore, the different vehicle load cases are applied to the basement structure for analyzing the damage situation in comparison with the damage indicator mentioned in Section 3.1. The vehicle loads are placed in the middle of the travelling lane on both Y-direction (between Axis 18 and Axis 19) and X-direction (between Axis C and Axis D) roof plates, as illustrated in Figure 7a,b, respectively. The positions of the vehicle loads are indicated by the green dots. In Figure 7a, the 40 t vehicle load is simplified to two concentrated forces of 20 t with a front-to-back distance of 7.6 m. It is assumed that the pullout resistance of the foundations for the 2h, 2i, 3h, 3i, 4h, 4i, 5h and 5i columns have failed and are represented as red squares. In Figure 7b, the vehicle load is simplified as four concentrated forces of 10 t with an up-down distance of 2.5 m and a front-to-back distance of 8 m. Additionally, it is assumed that the foundations for the 3c, 4c, 3d, 4d, 3f, 4f, 3g, 4g, 3h, 4h, 3i, 4i, 3j, 4j, 3k, 4k, 3m and 4m columns are subject to pullout force loss. Under these vehicle load cases, the internal forces, bending moments and maximum lateral displacements of some representative columns are calculated and listed in Tables 4 and 5, respectively.

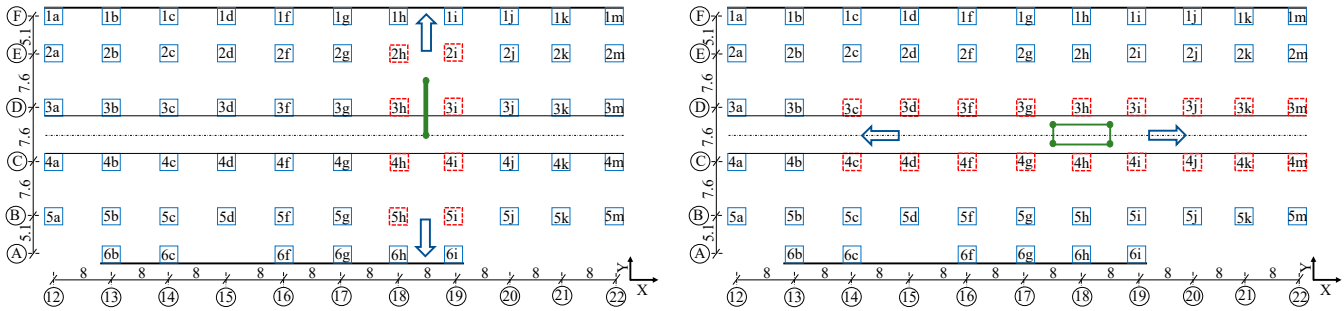


Figure 7. The vehicle loads and the pullout resistance state of the column foundations (Note: Green dots indicate the position of the vehicle loads. Red squares represent the failure of the pullout force of the column foundations. Blue squares denote the existence of the pullout force in the column foundations). (**a**) The vehicle loads in the Y-direction. (**b**) The vehicle loads in the X-direction.

Table 4. Forces, bending moments and maximum lateral displacements of the representative columns under the vehicle loads of the Y-direction.

Column No.	Axial Force (kN)	Stage 1 Cracking Moment (kN·m)	Stage 2 Cracking Moment (kN·m)	Stage 3 Bending Moment (kN·m)	Maximum Bending Moment of Column (kN·m)		Maximum Lateral Displacement (mm)
					Top	Bottom	
2h	482.16	65.57	70.38	217.82	49.42	13.25	0.33
2i	474.74	70.81	75.43	225.39	48.04	12.10	0.27
4h	522.14	75.82	81.67	232.97	38.49	33.71	0.63
4i	557.29	79.82	85.86	238.67	22.90	28.00	0.92

In Table 4, it is observed that the maximum bending moments at the top and bottom of the columns are 49.42 kN·m and 33.71 kN·m, respectively, when the vehicle loads act on the travel lane of the roof plate between Axis 18 and Axis 19 in the Y-direction. Neither of these values has yet reached their corresponding Stage 1 cracking moment, indicating no generation of cracks. However, it can be inferred that vehicle loads have a greater impact on the bending moment at the column top than at the column bottom. From Table 5, it can be observed that the bending moment at the top of the 3g column exceeds its Stage 1 cracking moment under the vehicle loads between Axis C and Axis D in the X-direction. The Level B cracks occur at the top of the 3g column, which is referenced as T-2B on 3g column in

Figure 2. Specifically, the bending moment is measured at 59.69 kN·m while the Stage 1 cracking moment is only 57.16 kN·m. Consequently, small cracks may appear at the top of this column but no cracks are visible at its bottom. Similarly, for the 5g column, its bending moment reaches up to 78.93 kN·m which represents approximately 93% of its corresponding Stage 1 cracking moment (84.77 kN·m). The initiation of cracks will occur at the top of the 5g column (T-2D on 5g column). It is evident that all other bending moment values are inferior to their corresponding Stage 1 cracking moments, thus resulting in cracks at these positions along the columns.

Table 5. Forces, bending moments and maximum lateral displacements of the representative columns under the vehicle loads of X-direction.

Column No.	Axial Force (kN)	Stage 1 Cracking Moment (kN·m)	Stage 2 Cracking Moment (kN·m)	Stage 3 Bending Moment (kN·m)	Maximum Bending Moment of Column (kN·m)		Maximum Lateral Displacement (mm)
					Top	Bottom	
3g	353.70	57.16	61.37	206.54	59.69	38.61	0.883
3m	448.04	67.27	71.78	221.60	52.81	32.00	1.361
4f	682.03	91.62	98.84	255.74	72.78	38.73	1.602
5g	605.84	84.77	91.21	246.27	78.93	33.80	0.350

3.3. Antifloating Failure Model of the Basement

With the advancement of antifloating measures for the damaged columns, an increased occurrence of cracks at both the top and bottom sections have been observed. In this section, a model for antifloating failure is constructed as depicted in Figure 8. The red squares labeled in Figure 8 indicate that the restraints at the bottom of the 3c, 4c, 5c, 2d, 3d, 4d, 2f, 3f, 4f, 2g, 3g, 4g, 5g, 2h, 3h, 4h, 5h, 2i, 3i, 4i, 5i, 4j, 3k, 4k and 4m columns have been released to simulate pullout resistance failures.

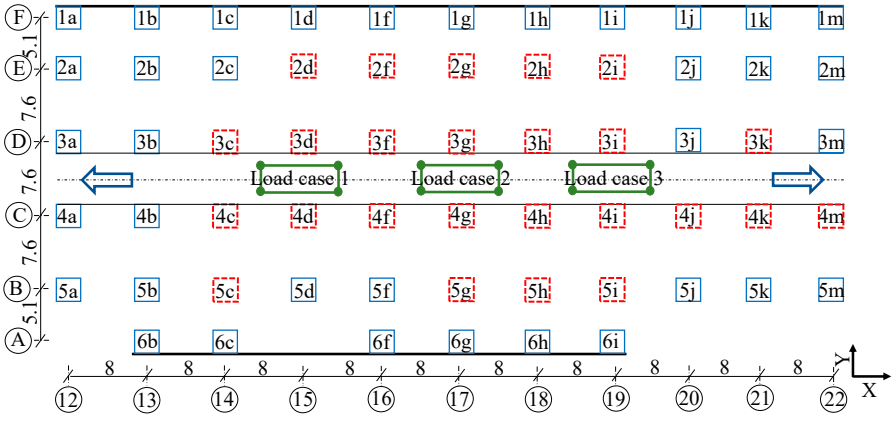


Figure 8. The pullout force failure of the columns.

In the antifloating failure model, three different positions in the X-direction between Axis C and Axis D on the travel lane of the top slab are loaded with the vehicle loads of 40 t, which are identical to those shown in Figure 7b. Load case 1 involves four concentrated forces of 10 t at the left end of the travel lane between 3c, 3f, 4c and 4f. Load case 2 applies the vehicle loads in the middle of the travel lane between 3f, 3h, 4g and 4h. Load case 3 represents a scenario where the vehicle loads are shifted towards the right end of the travel lane, specifically between 3h, 3j, 4h and 4j. In contrast, Load Case 4 does not involve any vehicle loads. The resulting axial forces, bending moments and maximum lateral displacements for each column can be obtained in Table 6.

Table 6. Axial forces, bending moments and maximum lateral deformations of the 2 g and 4 g columns under various load cases.

Load Cases	Column No.	Axial Force (kN)	Stage 1 Cracking Moment (kN·N)	Stage 2 Cracking Moment (kN·m)	Stage 3 Bending Moment (kN·m)	Maximum Bending Moment of The Column (kN·m)		Maximum Lateral Displacement (mm)
						Top	Bottom	
Load case 1	2g	308.01	50.65	53.95	199.08	160.66	156.83	4.573
	4g	617.24	85.50	92.14	248.16	131.30	106.01	2.217
Load case 2	2g	299.74	50.15	53.15	198.08	173.12	169.74	4.025
	4g	690.50	91.62	98.94	255.74	140.61	117.43	0.568
Load case 3	2g	307.52	50.65	53.95	199.08	157.68	154.26	4.498
	4g	618.69	86.25	93.08	248.16	131.38	106.83	1.936
Load case 4	2g	307.80	50.65	53.95	199.08	136.21	133.27	4.846
	4g	620.56	86.25	93.08	248.16	86.50	78.41	2.816

From Table 6, it can be observed that the maximum bending moments of the 2g and 4g columns exceed their corresponding stage 2 cracking moment when the vehicle loads move from left to right on the travel lane of the top slab between Axis C and Axis D. However, these maximum bending moment values do not surpass their corresponding stage 3 bending moments. Even the maximum bending moments of the 2g column in Load case 4 fall within the range between the corresponding stage 2 cracking moment of 53.95 kN·m and yield bending moments of 199.08 kN·m (B-5C, B-3B and T-1B on the 2g column). However, for the 4g column in Load case 4, its maximum bending moments are either close to or less than its corresponding stage 1 cracking moment of 86.25 kN·m (T-2C and B-4C on 4g column). These findings suggest that the columns have experienced severe cracking under vehicle loads and belong to Level C in terms of crack severity. Nevertheless, their mechanical state remains intact within the elastic damage range, which is consistent with on-site observations of column damage.

Under these various load cases, the maximum uplift deformation of the basement can be obtained from Figure 9. It is evident from Figure 9 that the maximum uplift deformation of the basement is 0.191 m, which closely approximates the actual maximum uplift deformation of 0.194 m observed in situ. To further validate the effectiveness of the antifloating failure model, we have selected 30 damaged columns (including 2a to 2k, 3a to 3k and 4a to 4k) at Axis C to Axis E and compared their upward uplift displacements with actual measured values. The results are presented in Figure 10. As shown in Figure 10, the simulated uplift deformation values of the basement floor from the FE model are highly consistent with actual measurements. Based on Figure 10, it is evident that the modeled uplift deformation of the basement floor exhibits a high level of agreement with actual measured values, with maximum errors falling within 14%.

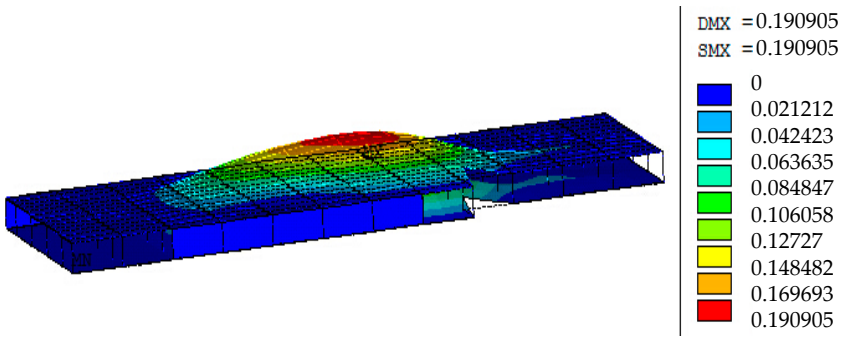
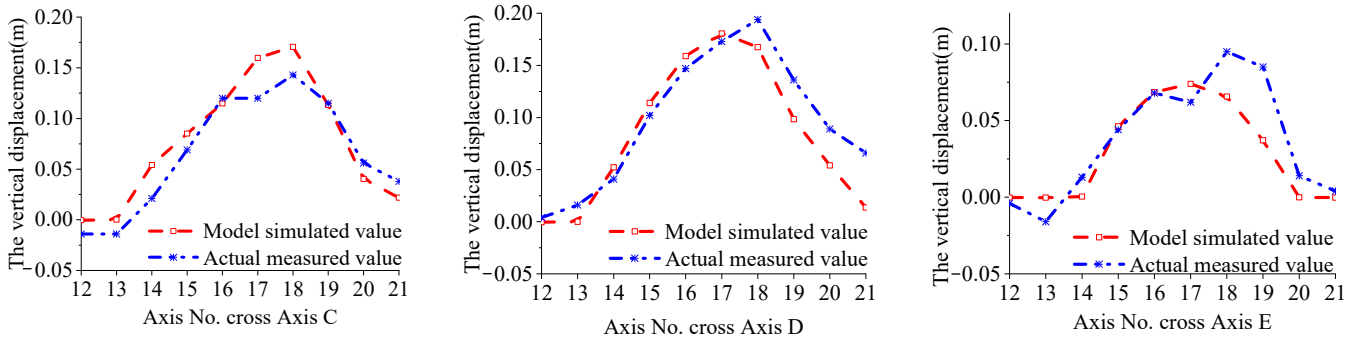


Figure 9. The uplift deformation of the basement (m).



(**a**) Axis C (**b**) Axis D (**c**) Axis E

Figure 10. The vertical displacement of the 30 damaged columns on the basement floor.

3.4. The Effect of the Weakened Concrete Strength

Due to limitatio ns in construction conditions, the actual strength grade of the concrete material falls short of its design value. Specifically, it is expected that the basement's concrete strength has weakened from C30 to C25. The failure model is the same as that of Load Case 4 in Section 3.3. The axial forces, bending moments and maximum lateral displacements for each column are obtained and listed in Table 7. From Table 7, it can be observed that the maximum bending moments of the 2g, 2h, 3g, 4f and 4g columns exceed their corresponding stage 2 cracking moment but fall short of the stage 3 bending moments. This indicates that these columns have experienced significant cracking, such as B-5C, B-3B, T-1B on 2g column, B-3D, T-2D on 2h column, T-2B, B-4B on 3g column, T-2B, B-4B on 4f column, T-2C, B-4C on 4g column.

Table 7. Axial forces, bending moments and maximum lateral displacements of the representative columns with the weakened concrete.

Column No.	Axial Force (kN)	Stage 1 Cracking Moment (kN·N)	Stage 2 Cracking Moment (kN·m)	Stage 3 Bending Moment (kN·m)	Maximum Bending Moment of Column (kN·m)		Maximum Lateral Displacement (mm)
					Top	Bottom	
2g	307.80	50.65	53.95	199.08	173.12	169.74	4.846
2h	450.53	68.43	73.22	226.60	75.03	98.81	2.728
3g	356.81	57.16	61.37	206.54	75.92	66.48	7.909
4f	677.64	91.62	98.94	255.74	155.72	121.26	1.406
4g	620.56	86.25	93.08	248.16	140.61	117.43	2.816

3.5. The Bending–Shear Failure Modes of the Side Columns

The side columns of the basement will be impacted by the shear walls. The conditions are the same as that of Section 3.4, the bending moments, shear forces and maximum lateral displacements of the 1f, 1g, 1h, 1i and 6g columns are listed in Table 8. The results show that the maximum bending moments of the 1f, 1g and 1h columns exceed their corresponding stage 2 cracking moments indicating more severe cracks at their tops. These cracks are with respect to T-2D on 1f column, T-2D on 1g column, T-2D on 1h column, T-2D on 1i column, T-2C on 6g column.

The shear forces at the top and bottom of the side columns are relatively small. Although the maximum shear force, which is 46.96 kN, occurred at the top of the 1g column, it still satisfies the requirement for shear bearing capacity. Therefore, the antifloating failure caused by the groundwater buoyancy is identified as the primary reason for the destruction of side columns while the secondary cause can be attributed to the horizontal thrust generated from shear walls.

Table 8. The bending moments, shear forces and maximum lateral displacements of the side columns.

Column No.	Maximum Bending Moment of the Column Top (kN·m)	The Shear Force of the Column Top (kN)	The Shear Force of the Column Bottom (kN)	Maximum Lateral Deflections (mm)
1f	130.90	43.38	10.85	0.128
1g	137.72	46.96	13.42	0.128
1h	96.89	30.24	5.11	0.109
1i	43.39	6.67	20.64	0.110
6g	39.52	5.20	15.03	0.144

Due to limited space, only the more significant cracks are listed in the FE results. The main serious cracks were observed in the 2h, 2i, 3g, 4g, 4h, 4i, 5g, 5h, 5i and 6g columns, which were consistent with the actual cracks in the damaged area. Other minor cracks are attributed to the additional load effects, such as B-3A on 2c column, B-4A on 3c column, B-3A, B-2A on 4c column, B-2A on 5c column, B-3A on 2k column, B-1A on 3k column, B-3A, B-5B, on 4k column, B-3A, B-5A on 2m column, B-2A, B-1A on 3m column and B-1A on 4m column.

4. Investigation of the Up-Floating Destruction of the Basement

According to the mid-March site situation, local cracks were discovered in the basement. Subsequently, from May onwards, these cracks rapidly expanded and increased in quantity on a regional scale. Similar to the investigation in the literature [30], the district's external environment experiences a rainy season from May to June. However, the inadequate drainage facilities at the construction site result in a rapid and significant rise in groundwater levels during heavy rainfall. If the backfilled clay is not compacted enough or not backfilled into the basement in a timely manner, the rainwater and surface water may infiltrate the gap between the basement floor and the soil layer. Additionally, if the pullout resistance tests for pipe piles are not strictly enforced during preconstruction, and if the antifloating capacity of the basement structure is substandard, then once groundwater levels reach critical antifloating levels, there may be issues with pullout resistance. Additionally, there is a lack of strict enforcement on pullout resistance tests for pipe piles during pre-construction. In cases where the antifloating capacity of the basement structure falls below standard, the failure in basement foundation pullout resistance will occur once the groundwater levels reach critical antifloating levels, resulting in the uplifted and bulging basement floors.

During the construction period, the roof plate of the floating area serves as a temporary construction site where the concrete mixer trucks and other heavy-duty vehicles are active in this basement uplift area. Additionally, the construction materials are also stored in this region, which can cause a disruptive effect on the basement due to associated weights. These associated weights will have a disruptive effect on the basement. If there is insufficient tightness between the cushion cap of the column foundation and the pipe pile, and if the pipe piles fail to resist pulling forces, then this aforementioned disruptive action will result in greater damage to the connection between the cushion cap and the pipe pile. Meanwhile, the pulling resistance of the pipe pile foundation will be severely compromised, leading to a significant reduction in the overall antifloating capacity of the basement. As a result, the uplift failure of the basement is inevitable. With the groundwater levels rising rapidly, the column foundations with compromised pulling resistance will gradually increase and the cracks will continue to develop.

Based on the local failure state of the basement with respect to uplift and the model validation results presented in Section 3, the causes of the up-floating destruction in the basement are summarized:

(1) Due to the settlement effects, including the large water buoyancy and self-weight of high-rise residential buildings, the bending moments and shear forces occur at both the top and bottom of columns. However, the bending resistance at these positions is insufficient, resulting in horizontal cracks forming along the columns. In addition

to the horizontal cracks observed at the side columns, there are also oblique cracks present. These are indicative of the bending-shear-type damage that has occurred at the side columns.

(2) Due to the inadequate pullout resistance of the basement foundations, the floor slab experienced uplift damage due to water buoyancy force. Additionally, localized cracking was observed on both the floor and top slabs.

5. Reinforcement Model Validation and Measures

To reinforce and repair a basement structure that has suffered uplift destruction, it is common practice to stack heavy loads in the basement to balance the groundwater buoyancy and friction between the basement sidewalls and surrounding soil layers. This measure can restore the uplifted basement to its original position. However, it is important to check the bearing capacity of the basement floor beforehand to avoid damage.

Thus, the loading measures are conducted by laying a 150 mm thick layer of concrete and an 800 mm thick layer of casing soil on top of the basement's top slab. To simulate the reinforcement model, the water buoyancy force is applied to the basement floor, consistent with the conditions in Section 3. Two comparative cases are considered regarding whether or not the foundation of the basement loses pullout resistance. The bending moments and deformations of the basement are illustrated in Figures 11 and 12, respectively. As shown in Figure 11, the maximum moment of columns is 88.135 kN·m when column foundations possess sufficient pullout resistance. However, if there is a failure in pullout resistance, the maximum moment will escalate to 1020 kN·m. In Figure 12, the maximum vertical displacement of the basement is 5.314 mm under pullout resistance, while it increases to 65.931 mm once the partial restraints of column bases are released.

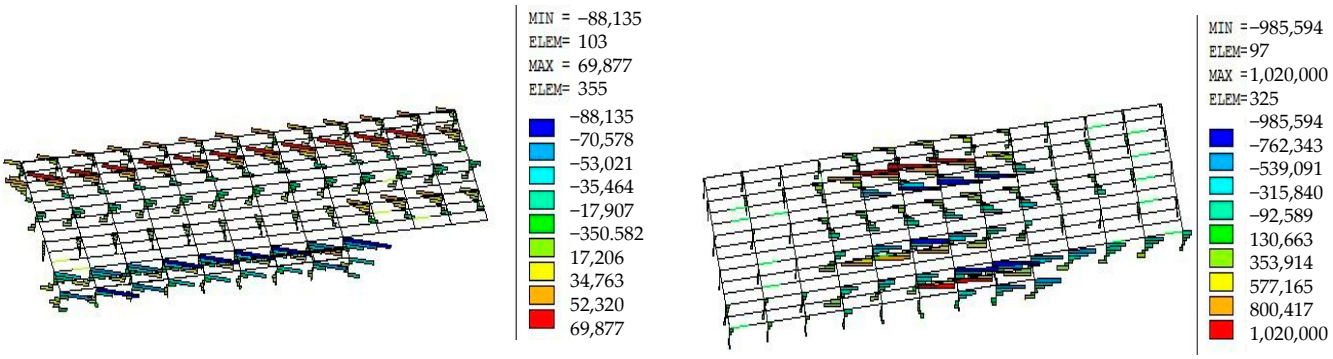


Figure 11. The bending moment of the columns after reinforcement (N·m). (**a**) Pullout resistance stabilization. (**b**) Pullout resistance failure.

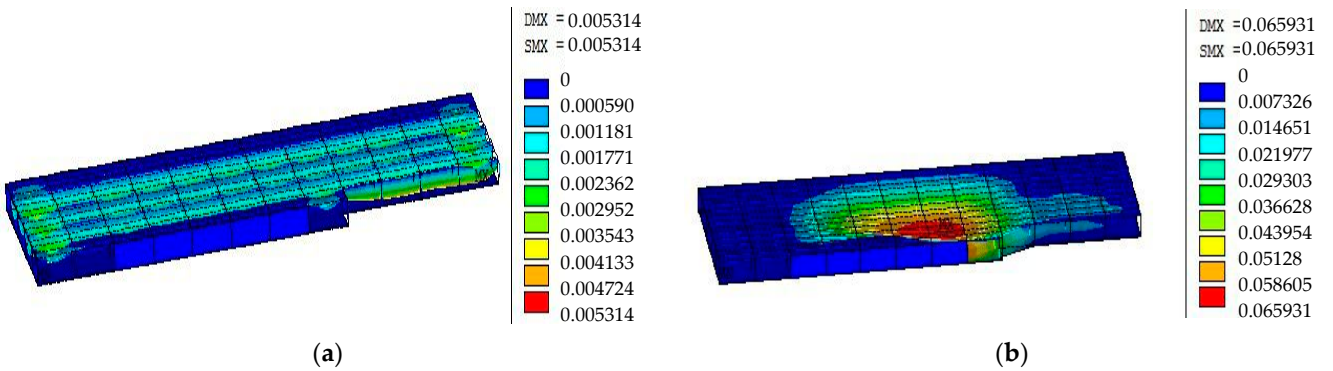


Figure 12. Vertical displacements of the basement structure after reinforcement (m). (**a**) Pullout resistance stabilization. (**b**) Pullout resistance failure.

In addition, the 150 mm thick concrete is poured onto the basement floor slab. The pullout resistance stabilization and failure scenarios are simulated to determine the bending moments of the floor slab, as depicted in Figure 13. From Figure 13, the maximum bending moment of the floor slab is 10.679 kN·m when all column bottoms are rigidly constrained. However, with the locally released constraints at the column bottoms, this value increases to 70.013 kN·m.

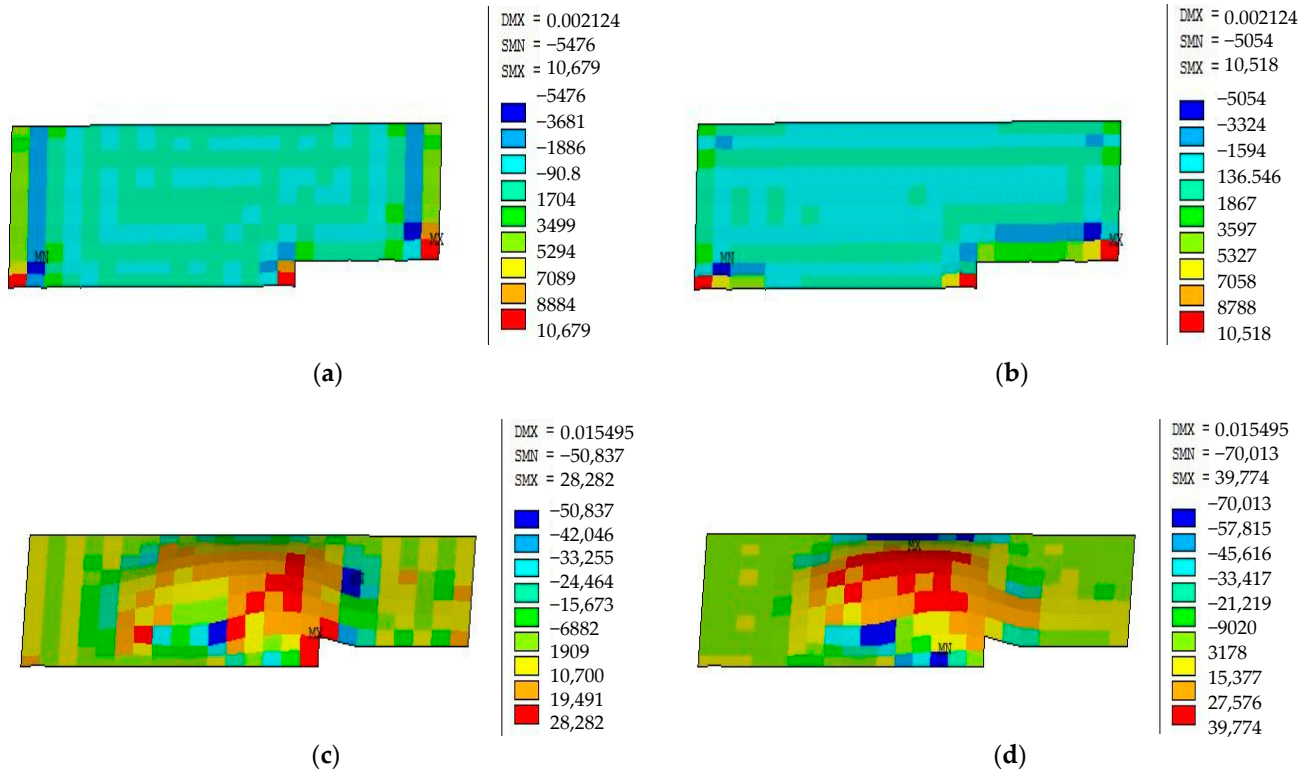


Figure 13. The bending moment of the floor slab after reinforcement (N·m). (**a**) M_x in the pullout resistance stabilization. (**b**) M_y in the pullout resistance stabilization. (**c**) M_x in the pullout resistance failure. (**d**) M_y in the pullout resistance failure.

Consequently, the general concept of "decompression first and then reinforcement" is proposed to address the up-floating destruction of the basement by combining several commonly used reinforcement measures [38] with the aforementioned reinforcement model. To ensure effective reinforcement of damaged areas and enhance overall building safety and reliability, specific corresponding measures are listed as follows:

(1) Reposition the water spillage holes in close proximity to the damaged columns [39]. The dimensions and locations of the designated water spillage holes are depicted in Figure 14. As shown in the figure, nine circular apertures with a diameter of 20 mm have been drilled and marked as red circles. These holes serve to alleviate the uplifting effect of water buoyancy on the basement floor by facilitating groundwater discharge. During the decompression period, it is necessary to regularly monitor the settlement of the bottom slab. Once the original groundwater has been released through the spillage holes, a sump pump should be used to drain any remaining open water and prevent backflow into the spillage holes.

(2) Plug the cracks in the components. Cracks in the columns, beams, slabs and walls require grouting treatment [40]. After sealing the cracks with grout, the carbon fiber sheets are utilized to reinforce the top slab surface as depicted in Figure 15.

(3) Reinforce the damaged columns with the U-shaped steel [41]. The U-shaped steel reinforcement measures for the side columns (KZ1) and main columns (KZ2) are

illustrated in Figures 16 and 17, respectively. The steel plates are installed between 650 mm below the bottom of the beam and 650 mm above the base plate.

(4) Thicken both the bottom and top slabs. The basement's bottom slab is filled with 150 mm thick concrete, which is connected to the original concrete using embedded steel bars as shown in Figure 18. After adding the overlay layer, to maintain the original design strength, it is necessary to incorporate a steel mesh into the laminated layer that matches or exceeds the size and spacing of steels in the original surface layer. The top slab is covered with casing soils that are 800 mm thick. According to structural FE calculation in Figures 11–13, these covered loads and the dead loads can meet the requirements of antifloating bearing capacity in the code [37]. Once the cover of the casing soils on the roof plate is fully installed, the spillage holes can be sealed.

(5) Install the drainage facilities. After completing all the aforementioned steps, the soils are backfilled and compacted thoroughly against the side walls. The implementation of measures to prevent drainage is also of significant importance.

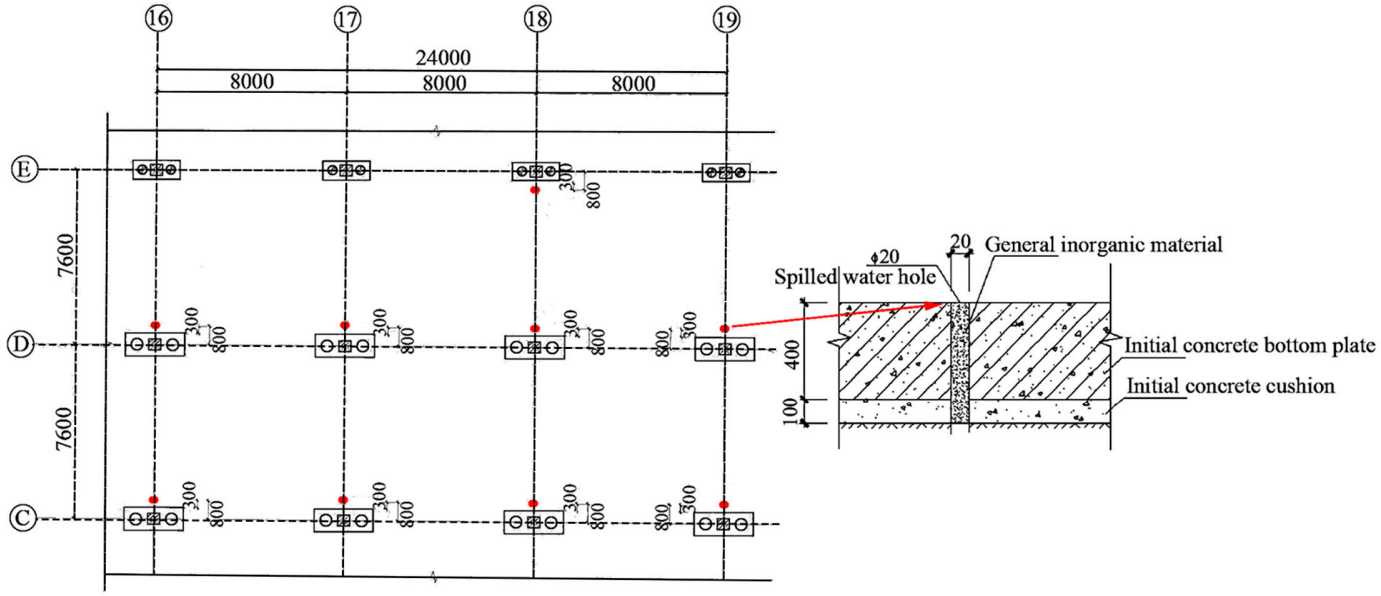


Figure 14. Pressure relief holes.

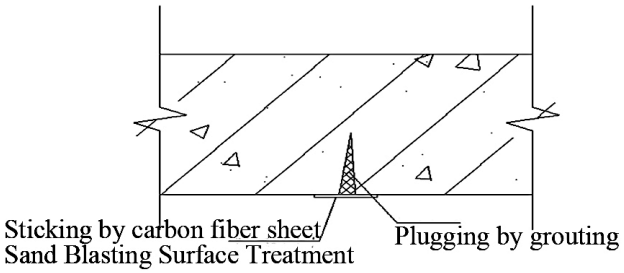


Figure 15. Crack sealing and reinforcement.

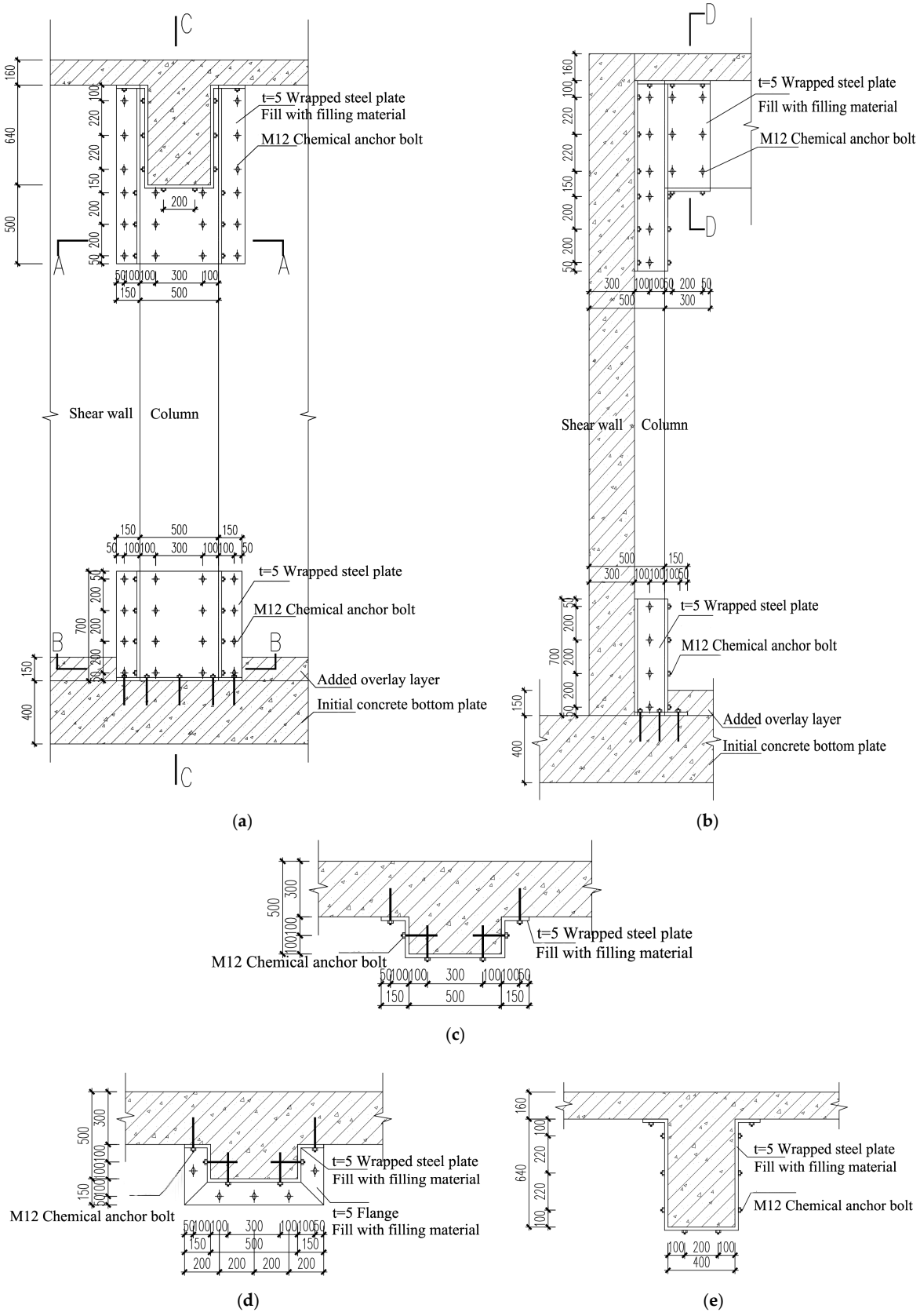


Figure 16. The reinforcement of the KZ1 side columns. (**a**) The reinforcement of the KZ1 side columns. (**b**) Cross profile of C-C. (**c**) Cross profile of A-A. (**d**) Cross profile of B-B. (**e**) Cross profile of D-D.

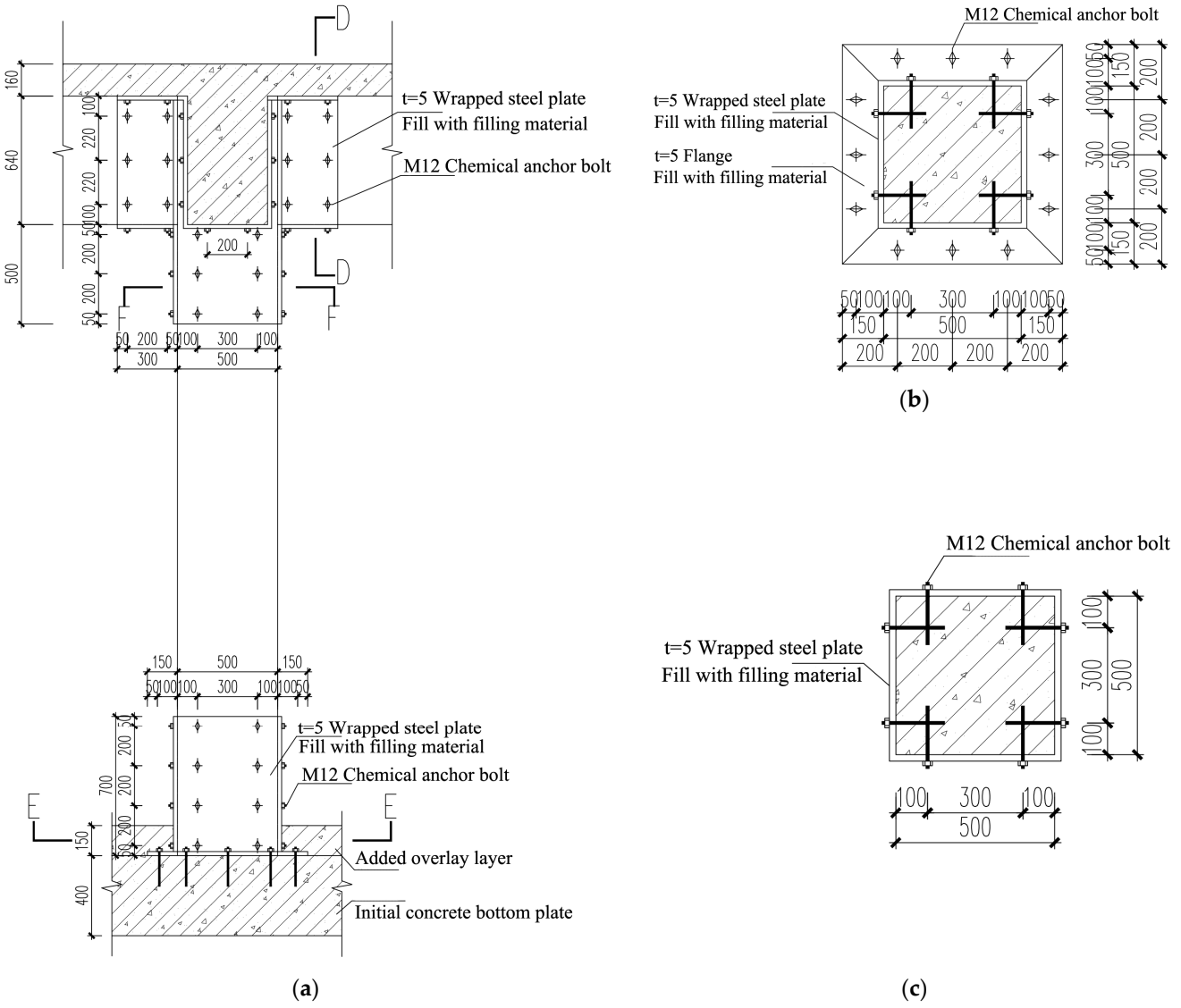


Figure 17. The reinforcement of the KZ2 columns. (**a**) The reinforcement of the KZ2 columns. (**b**) Cross profile of E-E. (**c**) Cross profile of F-F.

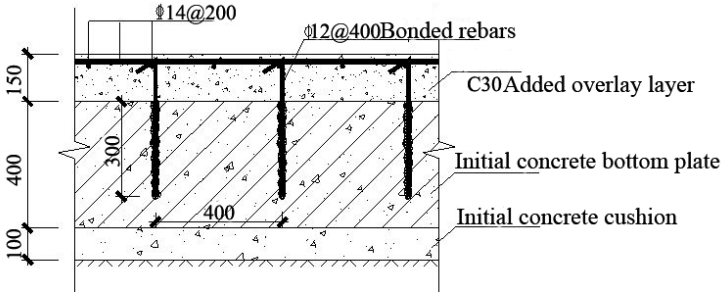


Figure 18. Reinforcement of the bottom slab.

6. Conclusions

In this paper, an FE model of the damaged basement structure subjected to the complex external forces including the water buoyancy forces and the vehicle loads is established by ANSYS. A novel damage indicator is proposed based on two levels of cracking bending moments and yield bending moments to assess the extent of structural damage. The

Stage 1, Stage 2 and Stage 3 bending moments at cracking and yield of the components can be determined using the section stratification method. When considering different vehicle loads and pullout resistance failure of basement foundations, the stress states and deformations of the basement can be compared with the stage bending moments to assess crack conditions. Finally, it was determined that the primary causes of up-floating destruction are: (1) the uplift effect resulting from the groundwater buoyancy force and the disruptive effects caused by vehicle loads and construction loads and (2) the pullout resistance failure of basement foundations.

The reinforcement strategy of "decompression first, then reinforcement" is proposed based on the up-floating destruction mechanism of the basement to repair and strengthen damaged structures. The effectiveness of the partial strategies is confirmed through a reinforcement model. The specific measures include: (1) positioning the spillage holes near the damaged columns; (2) sealing cracks in components with grouting and carbon fiber sheets; (3) reinforcing the damaged columns with U-shaped steel; (4) thickening the bottom and top slabs and (5) installing drainage facilities. These measures not only reduce construction costs but also meet structural safety requirements.

FE Model analysis in the investigation and reinforcement treatment of up-floating destruction can simulate the life cycle of emergence, development and treatment to ensure structural safety. The presented research ideas can serve as a reference for similar engineering accidents and minimize losses.

Author Contributions: Conceptualization, Z.W. and Z.L.; Data curation, Z.W. and B.H.; Formal analysis, Z.W. and B.H.; Funding acquisition, Z.L., J.F. and H.L.; Investigation, Z.L.; Methodology, Z.W. and J.F.; Project administration, Z.L., J.F. and H.L.; Resources, Z.L.; Software, Z.W. and B.H.; Supervision, Z.L., J.F. and H.L.; Validation, Z.W., Z.L. and H.C.; Visualization, Z.W. and Z.L.; Writing—original draft, Z.W.; Writing—review and editing, Z.W., Z.L., B.H., H.C. and H.L. All authors have read and agreed to the published version of the manuscript.

Funding: This research was funded by the National key research and development program of China (No. 2022YFC3802002), the Hainan Provincial Natural Science Foundation of China (No. 522CXTD517) and the Hubei Natural Resources Science and Technology Project (No. ZRZY2022KJ26). The support is gratefully acknowledged. Any opinions, findings, conclusions or recommendations expressed in this study are those of the authors and do not necessarily reflect the views of the sponsoring agencies.

Data Availability Statement: Data Availability Statement: All data, models or codes that support the findings of this study are available from the corresponding author upon reasonable request.

Conflicts of Interest: The authors declare no conflict of interest. The funders had no role in the design of the study; in the collection, analyses or interpretation of data; in the writing of the manuscript; or in the decision to publish the results.

References

1. Suppasri, A.; Pakoksung, K.; Charvet, I.; Chua, C.T.; Takahashi, N.; Ornthammarath, T.; Latcharote, P.; Leelawat, N.; Imamura, F. Load-resistance analysis: An alternative approach to tsunami damage assessment applied to the 2011 Great East Japan tsunami. *Nat. Hazard. Earth. Sys.* **2019**, *19*, 1807–1822. [CrossRef]
2. Chen, C.; Melville, B.W.; Nandasena, N.A.K.; Shamseldin, A.Y.; Wotherspoon, L. Experimental study of uplift loads due to tsunami bore impact on a wharf model. *Coast. Eng.* **2016**, *117*, 126–137. [CrossRef]
3. Saengtabtim, K.; Leelawat, N.; Tang, J.; Treeranurat, W.; Wisittiwong, N.; Suppasri, A.; Pakoksung, K.; Imamura, F.; Takahashi, N.; Charvet, I. Predictive analysis of the building damage from the 2011 Great East Japan tsunami using decision tree classification related algorithms. *IEEE Access* **2021**, *9*, 31065–31077. [CrossRef]
4. Wei, C.C. Collapse warning system using LSTM neural networks for construction disaster prevention in extreme wind weather. *J. Civ. Eng. Manag.* **2021**, *27*, 230–245. [CrossRef]
5. Ma, C.; Lu, D.C.; Du, X.L.; Qi, C.-Z.; Zhang, X.-Y. Structural components functionalities and failure mechanism of rectangular underground structures during earthquakes. *Soil. Dyn. Earthq. Eng.* **2019**, *119*, 265–280. [CrossRef]
6. Lu, L.; Qiu, J.; Yong, Y.; Tao, J.; Yu, H.; Wang, H.; Mang, H. Large-scale test as the basis of investigating the fire-resistance of underground RC substructures. *Eng. Struct.* **2019**, *178*, 12–23. [CrossRef]
7. Kelman, I.; Spence, R. An overview of flood actions on buildings. *Eng. Geol.* **2004**, *73*, 297–309. [CrossRef]

8. Drdacky, M.F. Flood damage to historic buildings and structures. *J. Perform. Constr. Fac.* **2010**, *24*, 439–445. [CrossRef]
9. Lazzarin, T.; Viero, D.P.; Molinari, D.; Ballio, F.; Defina, A. A new framework for flood damage assessment with time-evolving hazard, exposure, and vulnerability. *J. Hydrol.* **2022**, *615*, 128687. [CrossRef]
10. Jiang, W.Z.; Tan, Y. Overview on failures of urban underground infrastructures in complex geological conditions due to heavy rainfall in China during 1994–2018. *Sustain. Cities Soc.* **2022**, *76*, 103509. [CrossRef]
11. Polishchuk, A.I.; Chernyavskii, D.A.; Gumenyuk, V.V.; Solonov, G.G. Analysis of causes of underground and atmospheric water in basements of the building in operation. *Const. Geotech.* **2021**, *12*, 86–96. [CrossRef] [PubMed]
12. Vitali, O.P.M.; Celestino, T.B.; Bobet, A. Buoyancy effect on shallow tunnels. *Int. J. Rock. Mech. Min.* **2019**, *114*, 1–6. [CrossRef]
13. Ananev, A.A. Development of the Fastening Design of the underground structure immersed in water-satureted soils of St. Petersburg, from floating up. *Proced. Eng.* **2017**, *189*, 841–847. [CrossRef]
14. Wu, Y.X.; Yang, T.L.; Li, P.C.; Lin, J.-X. Investigation of groundwater withdrawal and recharge affecting underground structures in the Shanghai urban area. *Sustainability* **2019**, *11*, 7162. [CrossRef]
15. He, L.H.; He, Z.F. Analysis of floating effect of groundwater on built underground structure. *IOP Conf. Ser. Earth Environ. Sci.* **2021**, *784*, 012030. [CrossRef]
16. Zhang, J.W.; Cao, J.; Mu, L.; Wang, L.; Li, J. Buoyancy force acting on underground structures considering seepage of confined water. *Complexity* **2019**, *2019*, 7672930. [CrossRef]
17. Bikce, M.; Ornek, M.; Cansız, O.F. The effect of buoyancy force on structural damage: A case study. *Eng. Fail. Anal.* **2018**, *92*, 553–565. [CrossRef]
18. Zhu, L.; Peng, J.; Ren, Q. Analysis of the causes of cracks in the bottom floor of the underground garage of the Hefei Government affairs center by using 3D finite-element analysis. *J. Eng. Sci. Tech. Rev.* **2015**, *8*, 84–90. [CrossRef]
19. Maj, M.; Tamrazyan, A.; Ubysz, A. Considerable cracking in the foundation slab in a multi-storey underground garage. *MATEC Web Conf.* **2019**, *284*, 06003. [CrossRef]
20. Fu, Z.M.; Bai, Q. Discussion on anti-floating stability of tall building basement. In Proceedings of the 3rd International Conference on Advances in Energy and Environmental Science, Zhuhai, China, 25–26 July 2015; pp. 81–84. [CrossRef]
21. Maulik, R.A.; Upadhyaya, D.S.; Panchal, S.L. Preventation of hydrostatic uplift pressure underneath of basement floor slab in high water table area. *Int. J. Futur. Trends Eng. Technol.* **2014**, *1*, 72–75.
22. Wong, I.H. Methods of resisting hydrostatic uplift in substructures. *Tunn. Undergr. Sp. Tech.* **2001**, *16*, 77–86. [CrossRef]
23. Srivastava, A.; Babu, G.L.S. Uplift capacity and performance assessment of anchor piles installed to basement raft. *Electron. J. Geotech. Eng.* **2012**, *17*, 1173–1187.
24. Yang, L.H.; Wang, H.; Han, Z.G. Analysis and reinforcement on the up-floating accident of the basement of a large commercial complex. *Appl. Mech. Mater.* **2014**, *578–579*, 240–243. [CrossRef]
25. Zhu, D.F.; Cao, H.; Luo, G.Y.; Pan, H.; Mei, J.-L. Application of interception and drainage anti-floating system in treatment of uplift accidents. *Chin. J. Geotech. Eng.* **2018**, *40*, 1746–1752. [CrossRef]
26. Li, J.; Zhu, G.; Wang, J.; Zeng, P. Application of active anti-floating in underground structure based on automatic drainage system. *IOP Conf. Ser. Earth Environ. Sci.* **2021**, *636*, 012034. [CrossRef]
27. Tang, H.Y.; Yang, D.; Wang, C.J.; Guo, H.X.; Dong, Q.P. Anti-floating problem and retrofit measures for a damaged basement. *Mater. Res. Innov.* **2015**, *19*, 219–222. [CrossRef]
28. Zhang, Y. A Study on the Accident reason identification and reinforcement of the floated basement. In Proceedings of the International Conference on Engineering Science and Management, Zhengzhou, China, 13–14 August 2016. [CrossRef]
29. Huang, Y.H.; Pan, Z.B.; Luo, G.B.; Chen, L. Research on anti-floating reinforcement of an existing project. *IOP Conf. Ser. Mater. Sci. Eng.* **2020**, *758*, 012008. [CrossRef]
30. Tang, M.; Hu, H.; Zhang, C.; Hou, M.; Chen, H. Determination of anti-floating water level in Guangzhou based on the distribution of the underground aquifers. In Proceedings of the GeoShanghai 2018 International Conference: Geoenvironment and Geohazard, Shanghai, China, 27–30 May 2018. [CrossRef]
31. Wang, Z.; Liu, H. Analysis of the hydrogeological characteristics and aquifer structure in the southern area of Guangzhou. *Ground Water* **2011**, *4*, 79–81.
32. Li, Y.F.; Mu, L.L.; Cao, J. Impact of seepage on the underground water level in a complex soil-water-structure system. *Adv. Civ. Eng.* **2022**, *2022*, 7034778. [CrossRef]
33. Ni, P.; Kang, X.; Song, L.; Mei, G.; Zhao, Y. Model tests of buoyant force on underground structures. *J. Test. Eval.* **2019**, *47*, 1216–1235. [CrossRef]
34. Ren, Z.; Ni, P.; Mei, G. Time effect of buoyant force reduction for underground structures in clays: Model test and case study. *Inter. J. Geomech.* **2020**, *20*, 04020185. [CrossRef]
35. Zhou, J.K.; Lin, C.H.; Chen, C.; Zhao, X.Y. Reduction of groundwater buoyancy on the basement in weak-permeable/impervious foundations. *Adv. Civ. Eng.* **2019**, *2019*, 7826513. [CrossRef]
36. *GB/T 50010-2010*; Code for Design of Concrete Structures. China Building Industry Press: Beijing, China, 2015.
37. *GB/T 50009-2012*; Load Code for the Design of Building Structures. China Building Industry Press: Beijing, China, 2012.
38. *GB/T 50367-2013*; Code for Design of Strengthening Concrete Structure. China Building Industry Press: Beijing, China, 2013.
39. Ni, P.P.; Mei, G.X.; Zhao, Y.L. Antiflotation design for water tank using pressure relief technique. *Mar. Georesour. Geotechnol.* **2018**, *36*, 471–483. [CrossRef]

40. Matysek, P.; Witkowski, M. Analysis of the causes of damage to the RC floor slab in the underground garage. *MATEC Web Conf.* **2019**, *284*, 06004. [CrossRef]
41. Zhao, Y.; Yang, Y.; Xu, S.; Liu, J.; Chen, Y.F. Shear connection of reinforcement stiffened cold-formed U-shaped steel and concrete composite beam. *Eng. Struct.* **2020**, *219*, 110862. [CrossRef]

Disclaimer/Publisher's Note: The statements, opinions and data contained in all publications are solely those of the individual author(s) and contributor(s) and not of MDPI and/or the editor(s). MDPI and/or the editor(s) disclaim responsibility for any injury to people or property resulting from any ideas, methods, instructions or products referred to in the content.